Signature of chiral fermion instability in the Weyl semimetal TaAs above the quantum limit

Cheng-Long Zhang,[1] Bingbing Tong,[1] Zhujun Yuan,[1] Ziquan Lin,[2] Junfeng Wang,[2] Jinglei Zhang,[3] Chuan-Ying Xi,[3] Zhong Wang,[4,5] Shuang Jia,[1,5,*] and Chi Zhang[1,5,†]

[1]*International Center for Quantum Materials, Peking University, Beijing 100871, China*
[2]*National High Magnetic Field Center, Huazhong University of Science and Technology, Wuhan 430074, China*
[3]*National High Magnetic Field Laboratory, Chinese Academy of Science, Hefei 230031, China*
[4]*Institute for Advanced Study, Tsinghua University, Beijing 100084, China*
[5]*Collaborative Innovation Center of Quantum Matter, Beijing 100871, China*

(Received 17 January 2016; revised manuscript received 26 September 2016; published 11 November 2016)

We report the electrical transport properties for Weyl semimetal TaAs in an intense magnetic field. Strong temperature-dependent anomalies occur in the Hall signals and longitudinal magnetoresistance at low temperatures when the Weyl electrons are confined into the lowest Landau level. The temperature-dependent behaviors indicate that electron-hole pairing instability may be the origin of the anomalies. Our measurements show that the ultraquantum regime for the Weyl semimetals is not featureless.

DOI: 10.1103/PhysRevB.94.205120

A Weyl semimetal (WSM) is a topological material whose low energy excited states host the quasiparticles which obey the Hamiltonian for Weyl fermions [1,2]. A WSM provides an opportunity for studying the Weyl fermion which is well known in particle physics literature but has not been observed as a fundamental particle in vacuum. A WSM can be realized by breaking a time-reversal symmetry for Dirac semimetals in a magnetic environment. The semimetals without an inversion center on their crystal lattices are possible to host Weyl nodes [3,4], in which the Weyl nodes are the crossing points of a spin-splitted bulk band in momentum space. Weyl fermions appear as quasiparticles of their low-energy excitations near the nodes. Recently, the first nonmagnetic, noncentral symmetric WSM tantalum monoarsenide (TaAs) has been verified in experiments [5–8]. Angle-resolved photoemission spectroscopy (ARPES) experiments for TaAs observed Fermi arcs in its surface electronic states which connect the bulk Weyl nodes with opposite chiralities [7,8]. Electrical transport measurements in low magnetic fields detected negative longitudinal magnetoresistance (MR) which is ascribed to the Adler-Bell-Jackiw (ABJ) anomaly between the pairs of Weyl nodes [9–11]. Single crystals of TaAs also exhibit ultrahigh carrier mobilities and extremely large, linear transversal MR [11,12].

In this paper we focus on the electrical transport properties for TaAs in an intense magnetic field (B or $\mu_0 H$). A strong magnetic field can confine the electrons of a semimetal into the lowest Landau level (LLL), which is known as the QL as well [13–15]. A three-dimensional electron system in its QL exhibits one-dimensional metal characteristic effects [13,14]. Any small interaction can easily induce instabilities of the electrons in such highly degenerate states. Different types of instabilities in strong magnetic fields have been observed in topologically trivial semimetals [15–17], while prototype examples are charge density wave (CDW)-like phase transitions and excitonic phases in graphite [18–22]. On the other hand, the LLL for a WSM is topological nontrivial, it possesses two linear dispersive subbands which are separated in the momentum space. When an electric field is applied in the same direction as the magnetic field in this extremity, the charge in each chiral Landau subband is not conserved and the electrons are pumped from one to the other with opposite chirality [2,23–25]. In this simple scenario, a positive longitudinal magnetoconductivity will occur. However, it was claimed that the scattering may contribute positive or negative longitudinal magnetoresistance in the QL [26–28]. Electron interaction induced CDW, spin density wave (SDW), and excitonic phases are predicted for Weyl semimetals in theory as well, but these magnetic catalytic phase transitions were less considered [29–34]. The experiments for the WSM TaAs family are rarely reported in a magnetic field stronger than that in superconducting magnets [35,36]. All the referred complexities motivate us to study the electrical transport properties of the WSM TaAs beyond its QL.

Band structure calculations and ARPES experiments confirmed that TaAs has two types of Weyl nodes, four pairs of Weyl nodes 1 (W1) on $k_z = 2\pi/c$ (c is the lattice constant) plane and the other eight pairs of Weyl nodes 2 (W2) that are away from this plane [5–8]. In relation to the other three members (NbAs, NbP, and TaP) in the isostructural family [37,38], the single crystals of TaAs in general have smaller Weyl electron pockets with the maximal cross section area less than 10 T. The anisotropic Weyl electron pockets close to W1 have the maximal cross section area along the crystallographic c direction, which is three times smaller than that along the a direction. There also exists trivial pockets which have 2–5 times larger extremal cross section area than that of the pockets near W1 and W2 [5,7].

In order to comparably study the electrical properties in ultraquantum region with different directions of the electric field, we chose two single-crystalline samples of TaAs with different configurations: Sample S has the current along the a axis and the magnetic field along the c axis (configuration A: $H \parallel c$, $i \parallel a$), while sample C has the electric current and magnetic field parallel to the c axis (configuration B: $H \parallel i \parallel c$). Sample C was mainly measured in a He-3 fridge with a base temperature of 0.35 K in a static magnetic field as high as 35 T in the National High Magnetic Field Lab of China (NHMFLC)

*gwljiashuang@pku.edu.cn
†gwlzhangchi@pku.edu.cn

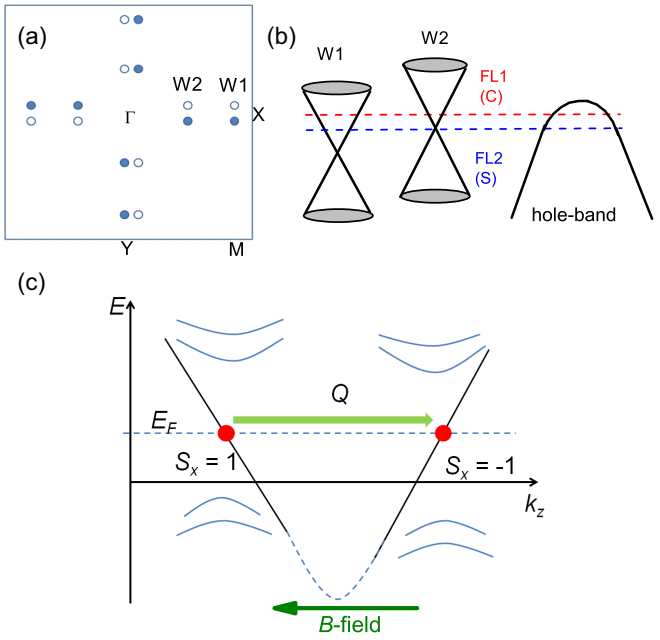

FIG. 1. (a) The schematic for the projection of all the Weyl points on the (001) surface of Brillouin zone for TaAs. (b) Fermi levels for samples S and C. (c) Sketch of the LLL of Weyl fermions and possible vector nesting between the Weyl points with opposite chirality.

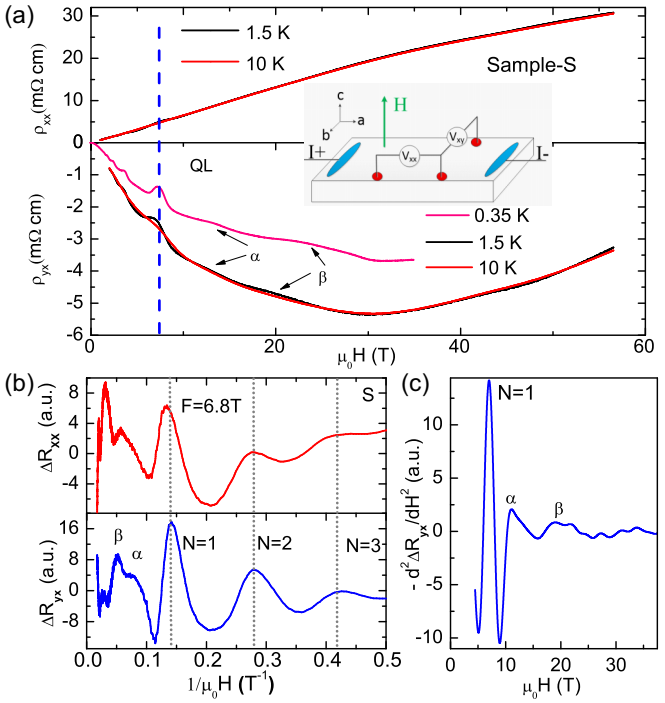

FIG. 2. Transport measurement results for sample S in configuration A. (a) ρ_{xx} and ρ_{yx} with respect to the field at 0.35 K (in a static field), and 1.5 and 10 K (in a pulsed field). Different data at 0.35 K and higher temperatures are due to the different setups in static and pulsed fields. The inset shows configuration A. (b) ΔR_{xx}, ΔR_{yx}, as the data at 1.5 K subtracted by the data at 10 K, with respect to the inverse field. (c) The derivative $-d^2\Delta R_{yx}/dH^2$ versus magnetic field is obtained from (b).

at Hefei. Besides the measurements in a static magnetic field, sample S was also measured in an environment with a base temperature of 1.5 K in a pulsed magnetic field as high as 55 T in NHMFLC at Wuhan.

Shubnikov–de Haas (SdH) oscillations with respect to the reciprocal of the magnetic field for both samples are shown in Figs. 1(b) and 2(b). The last few Landau levels are labeled as the peaks of the longitudinal resistance after subtracting the background (ΔR_{xx}) and the longitudinal resistivity (ρ_{zz}) for samples S and C, respectively. We observed a single frequency of 6.8 T for the SdH oscillations in ΔR_{xx} and the Hall signals after subtracting the background (ΔR_{yx}) for sample S. For sample C there are two sets of oscillations in ρ_{zz} with the frequencies equaling 9.5 and 7.5 T, respectively. Linear fitting of the Landau diagram shows intercepts very close to zero, indicating a nontrivial Berry phase [10,39]. Based on the band structure calculations we estimate that the chemical potential is located 13 meV above W1 for sample S where the electron pockets are eightfold degenerated. For sample C the chemical potential is located 18 meV above W1 and the two frequencies are from the extremal cross areas of the electron pockets near W1 and W2. A magnetic field stronger than 10 T is large enough to confine the electrons in the pockets near W1 and W2 to their LLL for both samples S and C.

The field-dependent transversal resistivity (ρ_{xx}) and Hall resistivity (ρ_{yx}) at 0.35, 1.5, and 10 K for configuration A are exhibited in Fig. 2. The values of ρ_{xx} are proportional to H below 30 T, while the curve of $\rho_{xx}(H)$ bends down very slightly above this field. The change of ρ_{xx} from 10 to 1.5 K is invisible beyond the QL. On the other hand, the slope of ρ_{yx} changes from negative to positive in a fixed field of 30 T at different temperatures (see more details in Appendix). Two small bumplike features occur at 14 and 25 T (labeled as α and β, respectively) in ρ_{yx} below 1.5 K but not at 10 K. The changes of ρ_{yx} for α and β are less than 2%.

The longitudinal resistivity in high magnetic fields show much richer features than ρ_{yx} and ρ_{xx} (Fig. 3). Disregarding the SdH oscillations which fade out at 15 K, negative field dependent ρ_{zz} of the sample C from 1 to 5 T persists at high temperatures. This part of negative contribution has been ascribed as an ABJ anomaly of the Weyl electrons [9]. The maximum of ρ_{zz} at the QL of 9 T is also robust at high temperatures when the SdH oscillations have faded out. Negative longitudinal MR beyond the QL was predicted for Weyl electrons due to a charge pumping effect [40,41].

Beyond the QL, ρ_{zz} has two local maxima at 13 and 22 T at 0.35 K, which are labeled as α and β, respectively. Two local minima at 15 and 26 T labeled as α' and β' follow α and β, respectively. The anomalies of α and β occur in the same fields as those on ρ_{yx} in configuration A. The anomalies of α and α' are invisible at 5 K, while those of β and β' persist at 15 K. Both of β and β' shift to higher fields with increasing temperature. Above 15 K, ρ_{zz} monotonically increases with field except the negative part of the contribution near the QL.

We plot β and β' for sample C in the diagram of the magnetic field and temperature [Fig. 4(a)]. Unlike the fixed field for the QL at 9 T, both of the fields for β and β' shift to high values with increasing temperature. The inset of Fig. 4 shows the values of ρ_{zz} at 12.7 and 26 T at different temperatures.

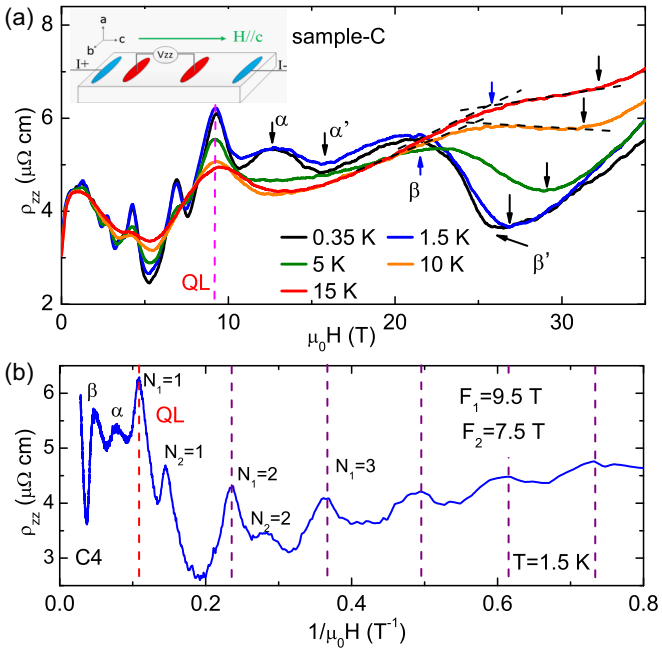

FIG. 3. Longitudinal resistance for sample C in configuration B. (a) ρ_{zz} with respect to the field at different temperatures. The inset shows configuration B. (b) ρ_{zz} with respect to the inverse field at 1.5 K.

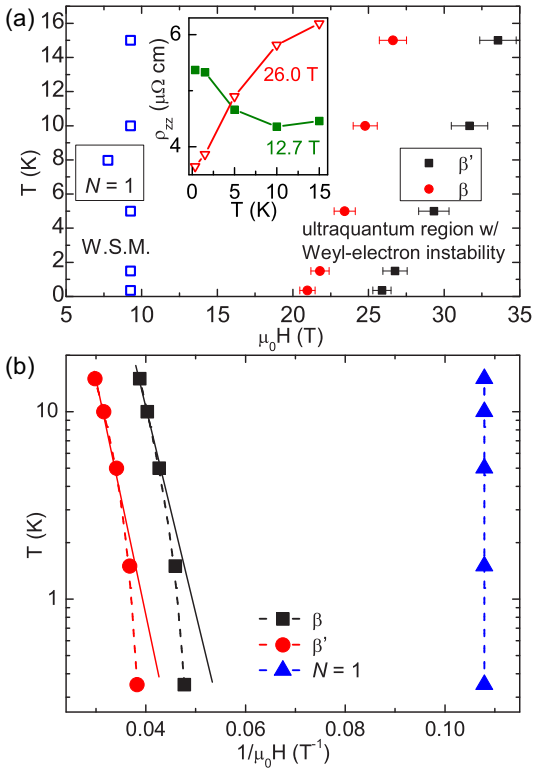

FIG. 4. (a) The anomalies of β and β' in ρ_{zz} and the QL for sample C are shown in the $\mu_0 H$-T plane. The inset shows the values of ρ_{zz} in 12.7 and 26.0 T at different temperatures. (b) β and β' and the QL are shown in the $1/\mu_0 H$-T plane.

At 12.7 T ρ_{zz} decreases with increasing temperature below 5 K while ρ_{zz} shows metallic temperature-dependent behavior above 26 T. It is noteworthy that the change of ρ_{zz} from 0.35 to 15 K in the ultraquantum region is much more significant than the change of the SdH oscillations below the QL.

A question then arises that what is the mechanism underneath these anomalies above the QL for TaAs. The temperature-dependent ρ_{zz} at 12.7 and 26 T and the changes of the fields for β and β' at different temperatures suggest that those anomalies are not likely due to an SdH oscillation from trivial pockets. The impurity scattering may induce the change of longitudinal MR above the QL, but the temperature dependence of the impurity scattering should not be so strong as what we observed from 0.35 to 5 K. The dramatic change of ρ_{zz} from 0.35 to 5 K indicates that those anomalies are related with some low-energy phenomena. A plausible explanation is that the interaction-induced instability may be present in TaAs. The instability of the electrons in the ultraquantum region has been investigated in graphite and bismuth [42]. Two magnetic field-catalyzed phase transitions due to the CDW-like, excitonic instability and depopulation of the Landau subband were observed beyond the QL of graphite [20,21]. These phase transitions induce moderate changes for the transversal MR and four orders of magnitude increase for the longitudinal MR [20]. On the other hand, the transversal MR for bismuth shows a weak anomaly far beyond the QL but the origin is still unclear with considering other different probe-adopted experiments [40,42]. Some similar features occurs in TaAs as well. The anomalies in the transversal signals are much smaller than those in the longitudinal signals. All of the anomalies induced by interactions occur at sufficiently low temperatures.

If we assume an electron-hole-pairing induced phase transition occurs in TaAs, the phase transition temperature T_C can be estimated as

$$T_C = \Lambda \exp\left[-\left(\frac{\hbar}{eB}\right)\frac{\hbar v_F}{ga^2c}\right] = \Lambda \exp\left(-\frac{B^\star}{B}\right) \quad (1)$$

in a mean-field approximation of BCS-type instability [14,33]. In this expression, Λ is a cutoff energy, which is typically the bandwidth of the Landau band, a and c are the lattice parameters, and g is the electron-electron interaction strength, which is estimated to be 1–2 eV. The Fermi wave vector along c axis $k_F = \sqrt{\frac{A_F}{\pi}}$ and the Fermi velocity v_F are estimated as 0.017 Å^{-1} and 1.31×10^5 m/s, respectively, by the analysis of the SdH oscillations. The characteristic magnetic field $B^* = (\frac{\hbar}{e})\frac{\hbar v_F}{ga^2c}$ from Eq. (1) is estimated as $\sim$ 195–390 T. This estimation is consistent with $B^* \sim 220$ T from the linear fit on the experimental data when $\Lambda \sim 10^4$ K.

In expression (1), T_C exponentially decays when $B \ll B^*$. As shown in Fig. 4(b), both temperatures for β and β' deviate from a linear relationship between $\ln T_\beta$, $\ln T_{\beta'}$, and the inverse magnetic field. The linear relationship of $\ln(T_C)$ vs $1/\mu_0 H$ was reported in pristine graphite, while for neutron-irradiated graphite the relation deviates from linearity which is similar as what we observed β or β' [43,44]. In neutron-irradiated graphite, the deviation is due to the pairing breaking effect by the charged impurities of the lattice defects which significantly affect its T_C.

Finally we show that the most plausible instability happening in TaAs is the SDW transitions with the nesting vector **Q** between the two Weyl pockets with opposite chirality. If the screened Coulomb interaction is responsible for the instability, the interaction should be stronger at smaller nesting vector. According to the previous band structure calculations and ARPES measurements, the nesting within each pair of Weyl points has the shortest distance from each other in the momentum space. As shown in Fig. 1(a), for a pair of W1 near the Brillouin zone boundary located at $(k_{0x}, \pm k_{0y}, 0)$, the nesting vector **Q** equals $(0, 2k_{0y}, 0)$ where $k_{0y} = 0.014\pi/a$ if W1 is initially located at the Fermi level [6]. In our samples whose Fermi level is away from the Weyl points, the Fermi points of the zeroth Landau level are shifted to $(k_{0x}, \pm k_{0y}, \pm k_{0z})$, where k_{0z} can be estimated from the SdH oscillation as $k_{0z} \approx 0.2\pi/c$, assuming that the chemical potential is fixed. The nesting vector is given by $\mathbf{Q} = (0, 2k_{0y}, 2k_{0z}) \approx (0, 0.03\pi/a, 0.2\pi/c)$. Due to the opposite spin quantum numbers at the two Fermi points, the instability will generates (see the Appendix) a helical spin density wave [34]. The cases of other three pairs of W1 Weyl points are similar. The same analysis is also applicable to the W2 Weyl points, whose instability generates helical spin density waves of different forms (see the Appendix). From our transport data at hand, it is difficult to distinguish the W1 instability from the W2 instability, and other experimental tools such as spin-resolved STM may be useful in further investigations.

The measurements for the Weyl semimetal TaAs family in an intensive field are less reported. A Hall signal reversal is reported for TaP while for NbAs the magnetic torque and resistance measurements show no additional features except the crossover from diamagnet to paramagnet above QL [10,45]. During the measurements we realize that the transport properties in magnetic field for the four compounds are very different. Considering the complicated band structure for TaAs, it is difficult to give a conclusive origin for these anomalies beyond the QL at this point. But their strong temperature dependence suggests the signs of the instability of Weyl electrons. And we think that the helical SDWs between the pairs of the Weyl electron pockets with opposite chiralities are the most plausible instability.

We would like to thank Fa Wang, Haiwen Liu and Su-Yang Xu for valuable discussions. C.L.Z. treats his research work as precious homework from Shui-Fen Fan. This project is supported by National Basic Research Program of China (Grants No. 2013CB921903 and No. 2014CB920904) and the National Science Foundation of China (Grant No. 11374020).

APPENDIX

1. Transport properties for TaAs at high temperatures

The magnetoresistance (MR) and Hall resistivity (ρ_{yx}) with respect to field at different temperatures are shown in Fig. 5. The slope change of ρ_{yx} in 30 T still occurs up to 100 K. At higher temperatures ρ_{yx} change its sign. A trivial hole conducting channel is likely the reason for this slope change. It is noteworthy that both of MR and ρ_{yx} change very little from

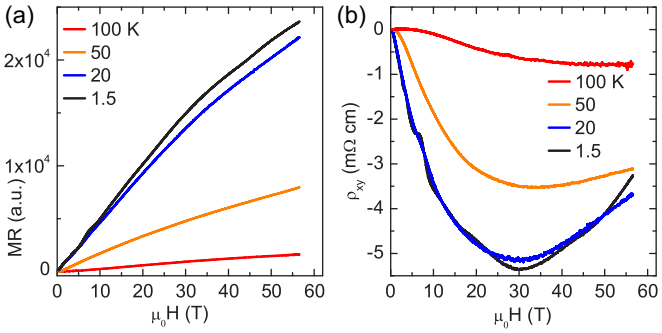

FIG. 5. Magnetoresistance and Hall resistivity with respect to field at different temperatures.

1.5 to 20 K, but the change becomes much more significant with respect to temperature above 20 K.

2. Nesting between Weyl electrons in TaAs and possible helical spin density waves

Suppose that the screened Coulomb interaction (which is stronger at smaller wave vector) is responsible for the instability towards the electron-hole pairing, we should look for small nesting vector **Q**. Therefore, we believe that the nesting within each pair of Weyl points with shortest distance from each other in the **k** space is responsible for the instability. There are two most probable inequivalent nesting vectors for the electron-hole instability, one of which comes from the W1 Weyl points and the other comes from the W2 Weyl points.

a. W1 Weyl points (Weyl points at the $k_z = 0$ plane)

According to symmetry analysis, an effective Hamiltonian near the two Weyl points around the Σ point can be obtained as

$$H(\mathbf{k}) = d_x\sigma_x + d_y\sigma_y + d_z\sigma_z + \lambda\sigma_y s_x, \qquad \text{(A1)}$$

where $\sigma_{x,y,z}$ describes the orbital degrees of freedom [6], and s_x is associated with the spin degree of freedom. Here $d_x(k) = uk_yk_z$, $d_y = vk_y$, $d_z = d_z(k_x)$. This leads to two Weyl points at $(k_{0x}, \pm k_{0y}, 0)$, where k_{0x} satisfies $d_z(k_{0x}) = 0$, $k_{0y} = \lambda/v$. The effective Weyl Hamiltonians near the two Weyl points are $H_W = v_x p_x\sigma_z + v_y p_y\sigma_y \pm v_z p_z\sigma_x$, where $v_x = \partial d_z/\partial k_x$, $v_y = v$, $v_z = \lambda u/v$. The two Weyl point has $s_x = \mp 1$ respectively.

According to Ref. [34], the zeroth Landau level wave function for the two Weyl points is $|s_x = -1, \sigma_x = 1\rangle$ and $|s_x = 1, \sigma_x = 1\rangle$, respectively. After the possible density wave transition (dynamical mass generation), we have the helical spin texture $s_y \sim \cos(\mathbf{Q}\cdot\mathbf{r} + \alpha)$ and $s_z \sim \sin(\mathbf{Q}\cdot\mathbf{r} + \alpha)$, where α is a constant. In this texture, the spin rotates in the s_y-s_z plane. It is a helical spin density wave (see Ref. [34]).

When the Weyl band-touching points is initially located at the Fermi level, we have $\mathbf{Q} = (0, 2k_{0y}, 0)$; if the Fermi level is away from the band-touching energy, the Fermi point of the two zeroth Landau level will be shifted to $\pm k_{0z}$, thus we have $\mathbf{Q} = (0, 2k_{0y}, 2k_{0z})$(Fig. 6). So far we have only considered a pair of Weyl points. There exist the other three pairs of Weyl points at the $k_z = 0$ plane, whose symmetry breaking

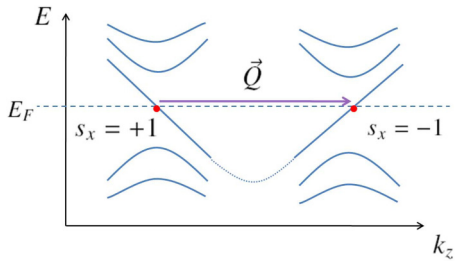

FIG. 6. Nesting between two W1 Weyl points. The wave vector $\mathbf{Q} = (0, 2k_{0y}, 2k_{0z})$. Here k_{0y} is mainly determined by the material itself, which can be read from the band structure of TaAs (see Ref. [6], $k_{0y} \approx 0.014\pi$), while k_{0z} is determined by the location of Fermi level (i.e., by doping).

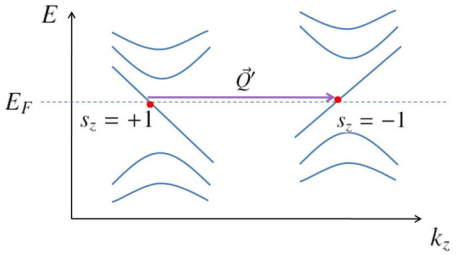

FIG. 7. Nesting between W2 Weyl points. The wave vector $\mathbf{Q}' = (0, 2k'_{0y}, Q'_z)$, where k'_{0y} is mainly determined by the material itself, which can be read from the band structure of TaAs (see Ref. [6], $k'_{0y} \approx 0.037\pi$), while Q'_z is determined by the chemical potential (i.e., by doping level). The Zeeman term shift the spectrum of the two Weyl point oppositely, which does not change the value of $\mathbf{Q}'$.

generates spin textures with other three values of $\mathbf{Q}$, namely, $(0, -2k_{0y}, 2k_{0z})$, $(\pm 2k_{0x}, 0, 2k_{0z})$, where $k_{0x} \equiv k_{0y}$.

Finally, we remark that the Zeeman term does not significantly change the picture. In fact, the Zeeman term is proportional to s_z, which is ineffective because the low-energy Weyl fermions have definite s_x value, and s_z mixes the low-energy fermions and "high-energy" fermions.

b. W2 Weyl points (located at $k_z \neq 0$ planes)

According to Ref. [6], the W2 Weyl points can be qualitatively described by

$$H(\mathbf{k}) = d_x\sigma_x + d_y\sigma_y + d_z\sigma_z + \lambda'\sigma_y s_z. \tag{A2}$$

The difference in the last term of Eqs. (A1) and (A2) is due to different symmetries at different points in the Brillouin zone, for instance, the $\lambda'\sigma_y s_z$ term is forbidden at the $k_z = 0$ plane.

Near one pair of Weyl points $(0, \pm k'_{0y}, k'_{0z})$, the low-energy Hamiltonian is completely similar to that of W1 Weyl points discussed in the previous section: $H_{\mathrm{W}} = v'_x p_x\sigma_z + v'_y p_y\sigma_y \pm v'_z p_z\sigma_x$. The only significant difference compared to the W1 Weyl points is that the two Weyl point has $s_z = \mp 1$ respectively (instead of $s_x = \mp 1$). The nonuniversal parameters $v'_{x,y,z}$ are, of course, different from $v_{x,y,z}$.

After possible pairing in the particle-hole channel, this pair of W2 Weyl point contribute a helical spin density wave $s_x \sim \cos(\mathbf{Q}' \cdot \mathbf{r} + \alpha)$ and $s_y \sim \sin(\mathbf{Q}' \cdot \mathbf{r} + \alpha)$. Here the wave vector $\mathbf{Q}' = (0, 2k'_{0y}, Q'_z)$ (Q'_z is determined by the chemical potential) (Fig. 7). Similar to the previous section, there are also other three values of $\mathbf{Q}'$ related by the crystal symmetries.

Due to the different physical parameters ($v_{x,y,z}$ and $\mathbf{Q}$), the transition in the W2 Weyl points occur at different magnetic field than the W1 Weyl points. This may be the reason of the existence of two peaks α and β in the experimental data.

[1] L. Balents, Weyl electron kiss, Physics **4**, 36 (2011).

[2] P. Hosur and X. Qi, Recent developments in transport phenomena in Weyl semimetals, C. R. Phys. **14**, 857 (2013).

[3] X. Wan, A. M. Turner, A. Vishwanath, and S. Y. Savrasov, Topological semimetal and Fermi-arc surface states in the electronic structure of pyrochlore iridates, Phys. Rev. B **83**, 205101 (2011).

[4] A. A. Burkov and L. Balents, Weyl Semimetal in a Topological Insulator Multilayer, Phys. Rev. Lett. **107**, 127205 (2011).

[5] S.-M. Huang, S.-Y. Xu, I. Belopolski, C.-C. Lee, G. Chang, B. Wang, N. Alidoust, G. Bian, M. Neupane, C. Zhang, S. Jia, A. Bansil, H. Lin, and M. Zahid Hasan, A Weyl Fermion semimetal with surface Fermi arcs in the transition metal monopnictide TaAs class, Nat Commun **6**, 7373 (2015).

[6] H. Weng, C. Fang, Z. Fang, B. A. Bernevig, and X. Dai, Weyl Semimetal Phase in Noncentrosymmetric Transition-Metal Monophosphides, Phys. Rev. X **5**, 011029 (2015).

[7] S.-Y. Xu, I. Belopolski, N. Alidoust, M. Neupane, G. Bian, C. Zhang, R. Sankar, G. Chang, Z. Yuan, C.-C. Lee, S.-M. Huang, H. Zheng, J. Ma, D. S. Sanchez, B. Wang, A. Bansil, F. Chou, P. P. Shibayev, H. Lin, S. Jia, and M. Zahid Hasan, Discovery of a Weyl Fermion semimetal and topological Fermi arcs, Science **349**, 613 (2015).

[8] B. Q. Lv, H. M. Weng, B. B. Fu, X. P. Wang, H. Miao, J. Ma, P. Richard, X. C. Huang, L. X. Zhao, G. F. Chen, Z. Fang, X. Dai, T. Qian, and H. Ding, Experimental Discovery of Weyl Semimetal TaAs, Phys. Rev. X **5**, 031013 (2015).

[9] D. T. Son and B. Z. Spivak, Chiral anomaly and classical negative magnetoresistance of Weyl metals, Phys. Rev. B **88**, 104412 (2013).

[10] C.-L. Zhang, S.-Y. Xu, I. Belopolski, Z. Yuan, Z. Lin, B. Tong, G. Bian, N. Alidoust, C.-C. Lee, S.-M. Huang, T.-R. Chang, G. Chang, C.-H. Hsu, H.-T. Jeng, M. Neupane, D. S. Sanchez, H. Zheng, J. Wang, H. Lin, C. Zhang, H.-Z. Lu, S.-Q. Shen, T. Neupert, M. Z. Hasan, and S. Jia, Signatures of the Adler–Bell–Jackiw chiral anomaly in a Weyl fermion semimetal, Nat. Commun. **7**, 10735 (2016).

[11] X. Huang, L. Zhao, Y. Long, P. Wang, D. Chen, Z. Yang, H. Liang, M. Xue, H. Weng, Z. Fang, X. Dai, and G. Chen, Observation of the Chiral-Anomaly-Induced Negative Magnetoresistance in 3D Weyl Semimetal TaAs, Phys. Rev. X **5**, 031023 (2015).

[12] C. Zhang, Z. Yuan, S. Xu, Z. Lin, B. Tong, M. Zahid Hasan, J. Wang, C. Zhang, and S. Jia, Tantalum monoarsenide: An exotic compensated semimetal, arXiv:1502.00251.

[13] B. I. Halperin, Possible states for a three-dimensional electron gas in a strong magnetic field, Jpn. J. Appl. Phys. **26**, 1913 (1987).

[14] V. M. Yakovenko, Metals in a high magnetic field: A universality class of marginal fermi liquids, Phys. Rev. B **47**, 8851 (1993).

[15] K. Behnia, Electron-hole pairing in presence of a strong magnetic field in graphite, JPSJ News Comments **12**, 05 (2015).

[16] K. Behnia, L. Balicas, and Y. Kopelevich, Signatures of electron fractionalization in ultraquantum bismuth, Science **317**, 1729 (2007).

[17] L. Li, J. G. Checkelsky, Y. S. Hor, C. Uher, A. F. Hebard, R. J. Cava, and N. P. Ong, Phase transitions of Dirac electrons in bismuth, Science **321**, 547 (2008).

[18] Y. Iye, P. M. Tedrow, G. Timp, M. Shayegan, M. S. Dresselhaus, G. Dresselhaus, A. Furukawa, and S. Tanuma, High-magnetic-field electronic phase transition in graphite observed by magnetoresistance anomaly, Phys. Rev. B **25**, 5478 (1982).

[19] D. Yoshioka and H. Fukuyama, Electronic phase transition of graphite in a strong magnetic field, J. Phys. Soc. Jpn. **50**, 725 (1981).

[20] B. Fauque, D. LeBoeuf, B. Vignolle, M. Nardone, C. Proust, and K. Behnia, Two Phase Transitions Induced by a Magnetic Field in Graphite, Phys. Rev. Lett. **110**, 266601 (2013).

[21] H. Yaguchi and J. Singleton, Destruction of the Field-Induced Density-Wave State in Graphite by Large Magnetic Fields, Phys. Rev. Lett. **81**, 5193 (1998).

[22] Y. Takada and H. Goto, Exchange and correlation effects in the three-dimensional electron gas in strong magnetic fields and application to graphite, J. Phys. Condens. Matter **10**, 11315 (1998).

[23] H. B. Nielsen and M. Ninomiya, The Adler-Bell-Jackiw anomaly and Weyl fermions in a crystal, Phys. Lett. B **130**, 389 (1983).

[24] E. V. Gorbar, V. A. Miransky, and I. A. Shovkovy, Chiral anomaly, dimensional reduction, and magnetoresistivity of Weyl and Dirac semimetals, Phys. Rev. B **89**, 085126 (2014).

[25] A. A. Zyuzin and A. A. Burkov, Topological response in Weyl semimetals and the chiral anomaly, Phys. Rev. B **86**, 115133 (2012).

[26] P. N. Argyres and E. N. Adams, Longitudinal magnetoresistance in the quantum limit, Phys. Rev. **104**, 900 (1956).

[27] S.-B. Zhang, H.-Z. Lu, and S.-Q. Shen, Linear magnetoconductivity in an intrinsic topological Weyl semimetal, New J. Phys. **18**, 053039 (2016).

[28] P. Goswami, J. H. Pixley, and S. Das Sarma, Axial anomaly and longitudinal magnetoresistance of a generic three-dimensional metal, Phys. Rev. B **92**, 075205 (2015).

[29] Z. Wang and S.-C. Zhang, Chiral anomaly, charge density waves, and axion strings from Weyl semimetals, Phys. Rev. B **87**, 161107 (2013).

[30] H. Wei, S.-P. Chao, and V. Aji, Excitonic Phases from Weyl Semimetals, Phys. Rev. Lett. **109**, 196403 (2012).

[31] H. Wei, S.-P. Chao, and V. Aji, Long-range interaction induced phases in Weyl semimetals, Phys. Rev. B **89**, 235109 (2014).

[32] B. Roy and J. D. Sau, Magnetic catalysis and axionic charge density wave in Weyl semimetals, Phys. Rev. B **92**, 125141 (2015).

[33] K.-Y. Yang, Y.-M. Lu, and Y. Ran, Quantum Hall effects in a Weyl semimetal: Possible application in pyrochlore iridates, Phys. Rev. B **84**, 075129 (2011).

[34] X.-Q. Sun, S.-C. Zhang, and Z. Wang, Helical Spin Order from Topological Dirac and Weyl Semimetals, Phys. Rev. Lett. **115**, 076802 (2015).

[35] C. Shekhar, A. K. Nayak, Y. Sun, M. Schmidt, M. Nicklas, I. Leermakers, U. Zeitler, Y. Skourski, J. Wosnitza, Z. Liu, Y. Chen, W. Schnelle, H. Borrmann, Y. Grin, C. Felser, and B. Yan, Extremely large magnetoresistance and ultrahigh mobility in the topological Weyl semimetal candidate NbP, Nat. Phys. **11**, 645 (2015).

[36] C. Zhang, Z. Lin, C. Guo, S.-Y. Xu, C.-C. Lee, H. Lu, S.-M. Huang, G. Chang, C.-H. Hsu, H. Lin, L. Li, C. Zhang, T. Neupert, M. Zahid Hasan, J. Wang, and S. Jia, Quantum phase transitions in Weyl semimetal tantalum monophosphide, arXiv:1507.06301.

[37] Y. Luo, N. J. Ghimire, M. Wartenbe, H. Choi, M. Neupane, R. D. McDonald, E. D. Bauer, J. Zhu, J. D. Thompson, and F. Ronning, Electron-hole compensation effect between topologically trivial electrons and nontrivial holes in NbAs, Phys. Rev. B **92**, 205134 (2015).

[38] C. Zhang, C. Guo, H. Lu, X. Zhang, Z. Yuan, Z. Lin, J. Wang, and S. Jia, Large magnetoresistance over an extended temperature regime in monophosphides of tantalum and niobium, Phys. Rev. B **92**, 041203 (2015).

[39] J. Hu, J. Y. Liu, D. Graf, S. M. A. Radmanesh, D. J. Adams, A. Chuang, Y. Wang, I. Chiorescu, J. Wei, L. Spinu, and Z. Q. Mao, π Berry phase and Zeeman splitting of Weyl semimetal TaP, Sci. Rep. **6**, 18674 (2016).

[40] J. Xiong, S. K. Kushwaha, T. Liang, J. W. Krizan, M. Hirschberger, W. Wang, R. J. Cava, and N. P. Ong, Evidence for the chiral anomaly in the Dirac semimetal Na_3Bi, Science **350**, 413 (2015).

[41] C. Zhang, H. Li, T.-R. Chang, S.-Y. Xu, W. Hua, H. Jiang, Z. Yuan, J. Sun, H.-T. Jeng, M. Zahid Hasan, X. C. Xie, and S. Jia, Ultraquantum magnetoresistance in single-crystalline β-Ag_2Se, arXiv:1502.02324.

[42] B. Fauque, B. Vignolle, C. Proust, J.-P. Issi, and K. Behnia, Electronic instability in bismuth far beyond the quantum limit, New J. Phys. **11**, 113012 (2009).

[43] Y. Iye, L. E. McNeil, and G. Dresselhaus, Effect of impurities on the electronic phase transition in graphite in the magnetic quantum limit, Phys. Rev. B **30**, 7009 (1984).

[44] K. Akiba, A. Miyake, H. Yaguchi, A. Matsuo, K. Kindo, and M. Tokunaga, Possible excitonic phase of graphite in the quantum limit state, J. Phys. Soc. Jpn. **84**, 054709 (2015).

[45] P. J. W. Moll, A. C. Potter, N. L. Nair, B. J. Ramshaw, K. A. Modic, S. Riggs, B. Zeng, N. J. Ghimire, E. D. Bauer, R. Kealhofer, F. Ronning, and J. G. Analytis, Magnetic torque anomaly in the quantum limit of the Weyl semi-metal NbAs, Nat. Commun. **7**, 12492 (2016).